Unique nature of the lowest Landau level in finite graphene samples with zigzag edges: Dirac electrons with mixed bulk-edge character

Igor Romanovsky,[*] Constantine Yannouleas,[†] and Uzi Landman[‡]
School of Physics, Georgia Institute of Technology, Atlanta, Georgia 30332-0430, USA
(Received 8 October 2010; published 27 January 2011)

Dirac electrons in finite graphene samples with zigzag edges under high magnetic fields (in the regime of Landau-level formation) are investigated with regard to their bulk-type and edge-type character. We employ tight-binding calculations on finite graphene flakes (with various shapes) to determine the sublattice components of the electron density in conjunction with analytic expressions (via the parabolic cylinder functions) of the relativistic-electron spinors that solve the continuous Dirac-Weyl equation for a semi-infinite graphene plane. Away from the sample edge, the higher Landau levels are found to comprise exclusively electrons of bulk-type character (for both sublattices); near the sample edge, these electrons are described by edge-type states similar to those familiar from the theory of the integer quantum Hall effect for nonrelativistic electrons. In contrast, the lowest (zero) Landau level contains relativistic Dirac electrons of a mixed bulk-edge character without an analog in the nonrelativistic case. It is shown that such mixed bulk-edge states maintain also in the case of a square flake with combined zigzag and armchair edges. Implications for the many-body correlated-electron behavior (relating to the fractional quantum Hall effect) in finite graphene samples are discussed.

DOI: 10.1103/PhysRevB.83.045421 PACS number(s): 71.70.Di, 73.22.Pr, 73.21.La, 73.43.Cd

I. INTRODUCTION

In the past few years, following the isolation of monolayer[1] and the fabrication of epitaxial[2] graphene, the physical properties of graphene nanostructures (including elongated graphene ribbons and finite graphene samples and flakes) have established themselves as a major research direction in condensed-matter physics. This development was propelled by theoretical predictions (see, e.g., Refs. 3–9) that the electronic properties of graphene nanostructures are strongly affected by the presence and termination character (in particular, zigzag or armchair) of the graphene edges, suggesting an unparalleled versatility and potential for future nanoelectronics applications. Crucial to the realization of this perspective is the capability to characterize and engineer edges with high purity and perfection, a need that has spurred an ever-expanding experimental effort which has already yielded highly promising results.[10–16]

In this context, a recent study[17] of ours addressed the influence of graphene edges on the properties of correlated many-body fractional-quantum-Hall-effect (FQHE) states of Dirac electrons. The most recent experimental observation[18–20] of such FQHE correlated states [in suspended monolayer[18,19] and bilayer[20] graphene samples under high magnetic fields (B)] has marked another milestone in demonstrating the potential of graphene not only for future technological applications but also for studying novel fundamental physics behavior. In particular, in Ref. 17 we showed that the Dirac-electron spinors in the lowest Landau level display a mixed bulk-edge character for graphene samples with zigzag edges, with the bulk component giving rise to the $\nu = 1/3$ FQHE state (but with an attenuated strength), while the edge component is responsible for the insulating behavior observed[18,19,21] at the Dirac neutrality point.

Naturally, the complexity of the computational many-body treatment of the interelectron repulsion necessitated the use in Ref. 17 of certain simplified assumptions, i.e., a circular shape for the graphene sample and an uninterrupted zigzag edge. In this article, motivated by the widespread and ongoing experimental activity on perfect-graphene-edge engineering (see above), we present a systematic study of the properties of Dirac-electron states (with respect to both their bulk-type and edge-type character) forming the Landau levels in graphene nanostructures with more realistic shapes[22–27] (namely flakes with triangular, hexagonal, and square shapes). To this end, we utilize a combination of tight-binding calculations on graphene flakes with analytic expressions (via the parabolic cylinder functions[28,29]) for the relativistic-electron spinors associated with the continuous Dirac-Weyl equation of a semi-infinite graphene plane.

We demonstrate that, away from the graphene-flake edge, the higher Landau levels contain exclusively electrons of a bulk-type character (for both sublattices); near the graphene-flake edge, these electrons are described by edge-type states reminiscent of those familiar from the theory of the integer quantum Hall effect for nonrelativistic electrons.[30] In contrast, the lowest (zero) Landau level of the graphene flakes contains relativistic Dirac electrons of a mixed bulk-edge character without an analog in the nonrelativistic case. It is shown that such mixed bulk-edge states maintain also in the case of a square flake with combined zigzag and armchair edges.

The article is organized as follows: Section II is devoted to the description of the methodologies employed. Specifically, Sec. II A derives the analytic expressions for the Dirac-Weyl spinors in the case of a semi-infinite graphene plane with zigzag edge termination; the solutions for both the K (Sec. II A 1) and K' (Sec. II A 2) graphene valleys are given. An outline of the tight-binding approach used here is given in Sec. II B. Our tight-binding results at high magnetic field (concerning the electron-density components of the two graphene sublattices and their interpretation through comparison with the continuum-model Dirac-Weyl spinors) are presented in Sec. III A for triangular flakes, Sec. III B

for hexagonal flakes, and Sec. III C for square flakes. Finally, Sec. IV offers a summary.

II. METHODOLOGY

A. Solutions of the Dirac-Weyl equation for a semi-infinite graphene plane

1. K valley

For a semi-infinite graphene plane under a perpendicular magnetic field B (with the graphene plane extending for $0 \leqslant x < \infty$ and exhibiting a zigzag edge along the y axis at $x = 0$), the Dirac-electron wave function corresponding to the K valley can be written as a two-component spinor (the zigzag boundary condition does not couple the two graphene valleys)

$$\psi(x,y) = \frac{e^{iq_y y}}{\sqrt{2}} \begin{pmatrix} \chi_A(x) \\ \chi_B(x) \end{pmatrix}. \tag{1}$$

In Eq. (1), $q_y = k_y - K_y$, with k_y, K_y being the linear momenta of the electron and the K valley along the y direction; the magnetic length $l_B = \sqrt{\hbar c/eB}$.

With the introduction of reduced (dimensionless) variables $x/l_B \to x$ and $x_c = q_y l_B$, the continuous Dirac-Weyl equation coupling the $\chi_A(x)$ and $\chi_B(x)$ components is given by

$$\frac{d}{dx}\chi_B + (x - x_c)\chi_B = \varepsilon \chi_A \tag{2a}$$

$$\frac{d}{dx}\chi_A - (x - x_c)\chi_A = -\varepsilon \chi_B, \tag{2b}$$

where the reduced energy $\varepsilon = E/(\hbar v_F/l_B)$, with v_F being the Fermi velocity of graphene.

In general, and prior to invoking any boundary conditions (that is considering the complete graphene sheet for $-\infty < x < \infty$), the solutions of the system of coupled equations in Eq. (2) fall into two classes, i.e., for $\varepsilon \neq 0$ and $\varepsilon = 0$.

Solutions for $\varepsilon \neq 0$. In this case, one can multiply both sides of Eq. (2b) with ε, and then use Eq. (2a) to eliminate χ_A. The result is the following second-order equation for χ_B:

$$\frac{d^2}{d\xi^2}\chi_B(\xi) + \left(\nu + \frac{1}{2} - \frac{1}{4}\xi^2\right)\chi_B(\xi) = 0, \tag{3}$$

where

$$\xi = \sqrt{2}(x - x_c) \quad \text{and} \quad \nu = \varepsilon^2/2. \tag{4}$$

Equation (3) has the standard form of a Weber differential equation, and thus its solutions coincide with the parabolic cylinder functions,[28,29,31] i.e.,

$$\chi_B(\xi) = C_\nu D_\nu(\xi), \tag{5}$$

where C_ν is a normalization constant.

Using Eq. (2a), the recurrence relation

$$\frac{d}{d\xi}D_\nu(\xi) + \frac{1}{2}\xi D_\nu(\xi) - \nu D_{\nu-1}(\xi) = 0, \tag{6}$$

and Eq. (4), the corresponding A component is given by:

$$\chi_A(\xi) = C_\nu \sqrt{\nu} D_{\nu-1}(\xi). \tag{7}$$

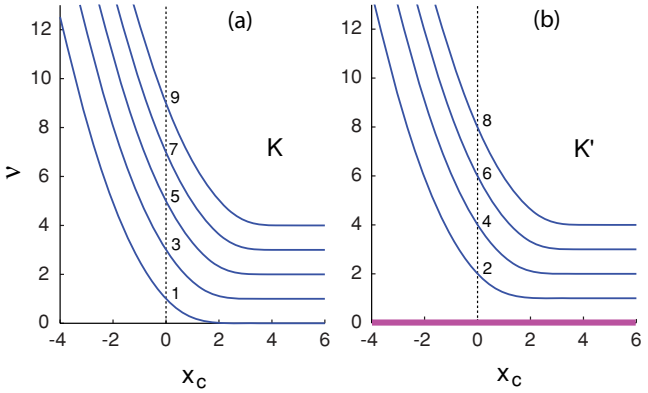

FIG. 1. (Color online) The eigenenergies (specifically the index ν) that solve the transcendental equation as a function of x_c (a) for the K valley [see Eq. (9)] and (b) for the K' valley [see Eq. (16)]. The almost flat segments of the curves correspond to Landau levels with energies $\varepsilon \approx \sqrt{2n}$, $n = 0, 1, 2, \ldots$; the approximate symbol $\approx$ signifies that ν does not take integer values but comes extremely close to them. The rising-in-energy branches correspond to double-edge states (i.e., states of edge character on both the A and B sublattices); they cross the vertical axis at $x_c = 0$ for (a) odd integer values and (b) even integer values. Note that the K valley (a) exhibits a dispersive (varying with $x_c = q_y l_B$) quasiflat band with $\nu \approx 0$, while the K' valley (b) exhibits a dispersionless flat band with $\nu = 0$ [see text and thick line (magenta color online)]; this is the only case when ν takes an integer ($\nu = 0$) value.

When ν is a nonnegative integer, $n \geqslant 0$, the parabolic cylinder functions reduce to the familiar wave functions of the one-dimensional unconfined harmonic oscillator,

$$D_n(\xi) = 2^{-n/2} e^{-\xi^2/4} H_n\left(\frac{\xi}{\sqrt{2}}\right), \tag{8}$$

where H_n are Hermite polynomials. The wave functions in Eq. (8) have the property $D_n(\pm\infty) = 0$, appropriate for an unconfined harmonic oscillator; they also exhibit n zeros. When $\nu \neq n > 0$, $D_\nu(+\infty) = 0$, and for $\xi < 0$ an additional zero (compared to the case of $\nu = n$) develops, through which the parabolic cylinder function crosses the x axis and then develops an exponentially growing tail; an example for a state with (energy) $\nu = 2 + 9.229 \times 10^{-18}$ and $x_c = 7$ [see Fig. 1(a)] is given in Fig. 2. Specifically the number of zeros of $D_\nu(\xi)$ (with $\nu > 0$) is given by the ceiling function[32] $\lceil \nu \rceil$ (this includes the case when ν is a positive integer n); for $\nu \leqslant 0$, $D_\nu(\xi)$ has no zeros.

In the case of a semi-infinite graphene sheet with zigzag edges (extending for $0 \leqslant x < \infty$), one can require that the additional zero for the χ_B spinor component coincides with the origin of axes ($x = 0$); this provides the following transcendental equation for determining the energy levels of the Dirac electrons (remember that $\nu = \varepsilon^2/2$):

$$D_\nu(-\sqrt{2}x_c) = 0. \tag{9}$$

The single-particle energies ε [which are solutions of Eq. (9)] as a function of x_c are displayed in Fig. 1(a). One sees that Landau levels (with energy $\varepsilon \approx \sqrt{2n}$, $n = 0, 1, 2, \ldots$) are formed when the centroid x_c of the orbitals is far away from the

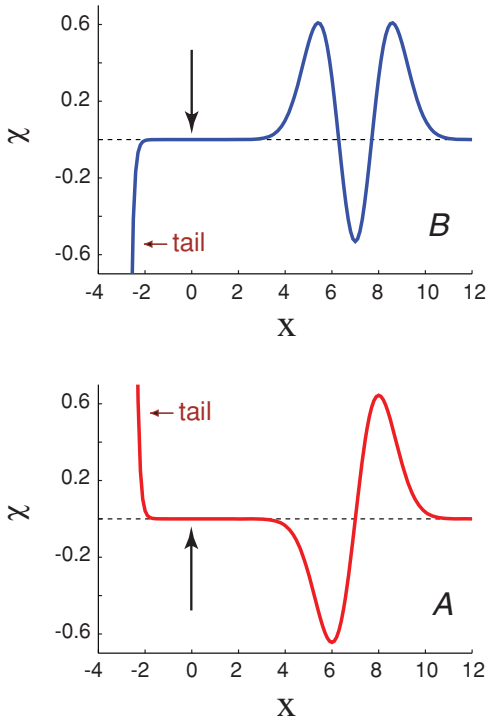

FIG. 2. (Color online) A bulk-bulk state in the third ($n = 2$) LL: The χ_B (top frame) and χ_A (bottom frame) Dirac-spinor components are displayed for $x_c = 7$ and $\nu = 2 + 9.229 \times 10^{-18}$ [see the transcendental Eq. (9)]. This state lies well inside the quasiflat segment of the third LL curve in Fig. 1(a). The vertical arrows mark the position of the boundary at $x = 0$. In the range $-\infty < x_c < 0$, note the development of exponentially growing tails, associated with the fact that the value of ν above is very close, but not equal, to an integer (here 2). Apart from the tails, both orbitals portrayed here are very close to the eigenfunctions of a 1D harmonic oscillator centered at x_c; see Eq. (8).

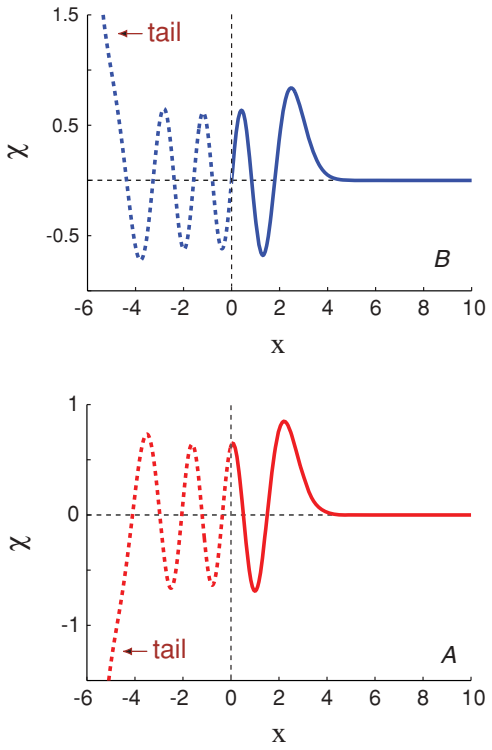

FIG. 3. (Color online) A double-edge state associated with the third ($n = 2$) LL: The χ_B (top frame) and χ_A (bottom frame) Dirac-spinor components are displayed for $x_c = -1$ and $\nu = 7.5266$ [see the transcendental Eq. (9)]. This state lies on the rising branch extending out from the flat segment of the third LL curve in Fig. 1(a). The vertical dashed lines mark the position of the physical boundary at $x = 0$. In the range $-\infty < x_c < 0$, note the development of exponentially growing tails, associated with the fact that the value of ν above is not equal to an integer. In the range $-\infty < x < +\infty$, the number of zeros associated with the B component is $\lceil \nu \rceil = 8$; for the A component it is $\lceil \nu - 1 \rceil = 7$. The physically relevant range $0 \leqslant x < +\infty$ contains only two zeros for both the cases of the B and A spinor components.

physical edge; the approximate symbol $\approx$ signifies that ν does not take integer values but comes extremely close to them. An illustrative case of the corresponding Dirac-spinor orbitals χ_B and χ_A are portrayed in Fig. 2. In the domain $-\infty < x < 0$, a tail develops due to the fact that the index ν is not an integer. In the physically relevant domain $0 \leqslant x < +\infty$, the two components are bulklike and very similar to the familiar wave functions of a 1D unconstrained harmonic oscillator. Similar orbitals (differing only in the number of zeros) apply for all Landau levels with $\nu \approx n \geqslant 1$.

For positive values of x_c near the boundary, and also for negative values of x_c, double-edge states are formed reminiscent of the single-edge states familiar from the theory of the integer quantum Hall effect.[30] The corresponding orbitals for an illustrative case (with $x_c = -1$ and $\nu = 7.5266$) are displayed in Fig. 3. Again, one sees the development of a tail in the domain $-\infty < x < 0$, due to the fact that the index ν is not an integer.

The case of large and positive x_c in the LLL ($n = 0$) is special and of particular significance regarding the strongly correlated Dirac-electron states in finite graphene samples under high magnetic field.[17] Indeed in this case, the Dirac spinor contains orbitals of both bulk and edge character. An illustrative case (with $x_c = 7$ and $\nu = 2.049 \times 10^{-21}$) is portrayed in Fig. 4. One sees that the B component is bulklike and similar to the ground state of a 1D harmonic oscillator in the physically relevant domain $0 \leqslant x < +\infty$. However, in the same domain, the A component is clearly edgelike.

Further understanding of this LLL behavior can be achieved through the observation that for $x_c \gg 0$ the LLL χ_A component can be approximated by

$$\chi_A^{\mathrm{LLL,app}}(x) \approx \widetilde{C} D_{-1}(\xi) = \widetilde{C} e^{\frac{1}{2}(x-x_c)^2} \sqrt{\frac{\pi}{2}} \mathrm{erfc}(x - x_c). \quad (10)$$

Taking into consideration that $\mathrm{erfc}(-x_c) \to 2$ for (large) $x_c \gg 1$, and keeping the lowest order in x/x_c in the exponent, one can determine the normalization constant $\widetilde{C}$. The final simplified expression is:

$$\chi_A^{\mathrm{LLL,app}}(x) = \sqrt{2x_c} e^{-x x_c}. \quad (11)$$

Equation (11) has the form of an exponential function decaying inside the graphene sheet. This form agrees very well with the full solution of χ_A in Fig. 4 [see Eq. (7) with $x_c = 7$

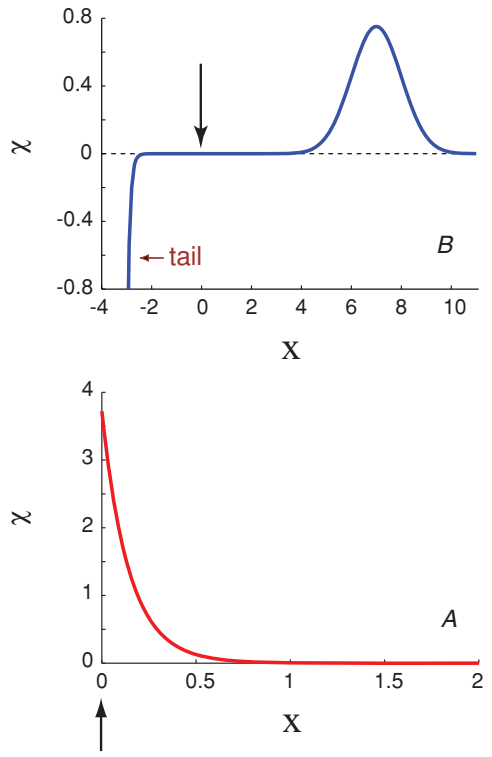

FIG. 4. (Color online) A bulk-edge state in the LLL ($n = 0$): The χ_B (top frame) and χ_A (bottom frame) Dirac-spinor components are displayed for $x_c = 7$ and $\nu = 2.049 \times 10^{-21}$ [see the transcendental Eq. (9)]. This state lies well inside the quasiflat segment of the LLL curve in Fig. 1(a). The vertical arrows mark the position of the boundary at $x = 0$. In the top frame, note the development (in the range $-\infty < x_c < 0$) of an exponentially growing tail, associated with the fact that the value of ν above is very close, but not equal, to an integer (here 0). Apart from the tail, the orbital portrayed in the top frame is very close to the ground-state eigenfunction of a 1D harmonic oscillator centered at x_c; see Eq. (8).

and $\nu = 2.049 \times 10^{-21}$]. We note that the surface character of this edgelike LLL A-component becomes more pronounced (i.e., it exhibits a narrower $1/x_c$ width) the larger the (positive) value of the centroid x_c.

Solutions for $\varepsilon = 0$. In this case, the two equations in Eq. (2) decouple, yielding the two solutions

$$\chi_B(\xi) = C_B e^{-\xi^2/4} \tag{12a}$$
$$\chi_A(\xi) = 0, \tag{12b}$$

and

$$\chi_B(\xi) = 0 \tag{13a}$$
$$\chi_A(\xi) = C_A e^{\xi^2/4}. \tag{13b}$$

For the nontrivial case (C_A or $C_B \neq 0$), neither of these two solutions satisfy the boundary conditions $\chi_B(-\sqrt{2}x_c) = 0$ and $\chi_B(+\infty) = \chi_A(+\infty) = 0$. Thus there is no dispersionless solution with $\varepsilon = 0$ associated with the K valley. However, as we will see below, such $\varepsilon = 0$ solutions exist for the K' valley.

2. *K′ valley*

The continuous Dirac-Weyl equation coupling the $\chi'_A(x)$ and $\chi'_B(x)$ components in graphene's K' valley is given by

$$\frac{d}{dx}\chi'_B - (x - x_c)\chi'_B = -\varepsilon(-\chi'_A), \tag{14a}$$
$$\frac{d}{dx}(-\chi'_A) + (x - x_c)(-\chi'_A) = \varepsilon\chi'_B. \tag{14b}$$

We note that Eq. (14) has the same form as Eq. (2) with the substitution $\chi_A \leftrightarrow \chi'_B$ and $\chi_B \leftrightarrow -\chi'_A$. As a result, for $\varepsilon \neq 0$, one has the following solutions for the Dirac spinor in the K' valley

$$\chi'_B(\xi) = C_\nu \sqrt{\nu} D_{\nu-1}(\xi) \tag{15a}$$
$$\chi'_A(\xi) = -C_\nu D_\nu(\xi), \tag{15b}$$

with the index $\nu = \varepsilon^2/2$ as was the case in the K valley.

The transcendental equation in the K' valley for the indices ν (or energies ε) as a function of x_c is written as

$$D_{\nu-1}(-\sqrt{2}x_c) = 0. \tag{16}$$

The solutions of Eq. (16) as a function of x_c are plotted in Fig. 1(b). Note that the index $\nu > 1$ in this case [$D_{\nu-1}(\xi)$ has no zeros for $\nu \leqslant 1$]. This contrasts with the case of the K valley shown in Fig. 1(a), where $\nu > 0$.

For $\varepsilon = 0$, the two equations in Eq. (14) decouple, and there is a physically valid solution

$$\chi'_A(\xi) = -C'_A e^{-\xi^2/4} \tag{17a}$$
$$\chi'_B(\xi) = 0. \tag{17b}$$

Assuming a relation $\nu = \varepsilon^2/2$, this dispersionless band of edge states can be associated with an index $\nu = 0$, and it is denoted by a thick dashed line in Fig. 1(b). This band maintains also for zero-magnetic field, since

$$\lim_{B\to 0} e^{-\xi^2/4} \propto e^{\tilde{x}q_y}, \tag{18}$$

which represents an edge state for $q_y < 0$; the tilded $\tilde{x}$ denotes the x position in the original dimensions of length (before the introduction of the reduced variable $x = \tilde{x}/l_B$; see Ref. 7).

B. Tight-binding approach for finite graphene flakes

In the tight-binding (TB) calculations, we use the Hamiltonian

$$H_{\rm TB} = -\sum_{\langle i,j\rangle} t_{ij} c_i^\dagger c_j + \text{H.c.}, \tag{19}$$

with $\langle\rangle$ indicating summation over the nearest-neighbor[33] sites i, j. The hopping matrix element

$$t_{ij} = t \exp\left(\frac{ie}{\hbar}\int_{\mathbf{r}_i}^{\mathbf{r}_j} d\mathbf{s}\cdot\mathbf{A}(\mathbf{r})\right), \tag{20}$$

where $t = 2.7$ eV, $\mathbf{r}_i$ and $\mathbf{r}_j$ are the positions of the carbon atoms i and j, respectively, and $\mathbf{A}$ is the vector potential associated with the applied perpendicular magnetic field B.

The calculations were carried out for two shapes that support a zigzag edge on all sides of the graphene flake, that is, equilateral triangles and regular hexagons, as well as for a square shape which exhibits both zigzag and armchair

edges. The number of carbon atoms considered is $N = 6397$ for the triangular flakes, $N = 6144$ for the hexagonal ones, and $N = 2074$ for the square one. The diagonalization of the TB Hamiltonian [Eq. (19)] is implemented with the use of the sparse-matrix solver ARPACK.[34]

III. RESULTS OF TIGHT-BINDING CALCULATIONS AND THEIR INTERPRETATION

A. Trigonal graphene flakes

In Fig. 5, we display the TB energies for the triangular flake with $\phi = 0.01$, $\phi = eSB/(\mathrm{hc})$ being the dimensionless magnetic flux through an hexagonal unit of the two-dimensional graphene lattice; S is the area enclosed by the hexagon and B is the magnetic field. The value $\phi = 0.01$ corresponds to a magnetic field sufficiently high so that Landau levels have been formed but at the same time low enough so that Hofstadter butterfly[35] effects (due to the periodicity of the lattice) have not developed.[23] The TB-energy curve in Fig. 5 exhibits a well-defined trend, i.e., several almost-flat horizontal segments are connected via fast-varying and rising-in-energy branches. The flat segments correspond to the Landau levels with energy $E/t \propto \mathrm{sign}(n)\sqrt{|n|}$, $n = 0, \pm1, \pm2, \ldots$.

A close inspection of the properties and behavior of the states associated with the TB energies in the $n = 0$ level reveals that this level contains two different bands: (i) a nondispersive one with energies close to the available machine precision ($E/t \sim 10^{-14}$) [that correspond to the $\varepsilon = 0$ solutions of the continuous model; see Sec. II A] and (ii) a quasidegenerate dispersive band with energies that are still very small (starting at $E/t \sim 10^{-8}$) but increase gradually and then merge with the rising-in-energy branch; this band corresponds [see the transcendental Eq. (9)] to the $\varepsilon \gtrsim 0$ solutions of the continuous model in the flat region of the lowest curve in Fig. 1(a). The nondispersive zero states coincide with the midgap surface states under field-free conditions and they have been studied extensively;[3–7,25] these states are not influenced by the magnetic field and will not be discussed any further here. The close-to-zero dispersive states are formed as a consequence of the external magnetic field, and they will be the primary focus of this article.

In Fig. 6, we display the TB electron densities (specifically the square root of the densities[36]) for states associated with the LLL in the case of a triangular graphene flake under the same magnetic field $\phi = 0.01$. The electron densities of the A (left, online red) and B (right, online blue) sublattices are plotted separately. Figures 6(a) and 6(b) correspond to TB states with energies ($E/t = 0.1699 \times 10^{-7}$ and $E/t = 0.1475 \times 10^{-3}$, respectively) that lie well inside the flat segment of the LLL ($n = 0$) energy curve in Fig. 5. It is apparent that these states are of a mixed bulk-edge character, with the B-sublattice component being bulklike and the A-sublattice component being edgelike. They are analogous to the mixed bulk-edge LLL states described in Sec. II A within the continuous relativistic Dirac-Weyl-equation framework. In particular, the spatial profile of the A-sublattice component of the TB

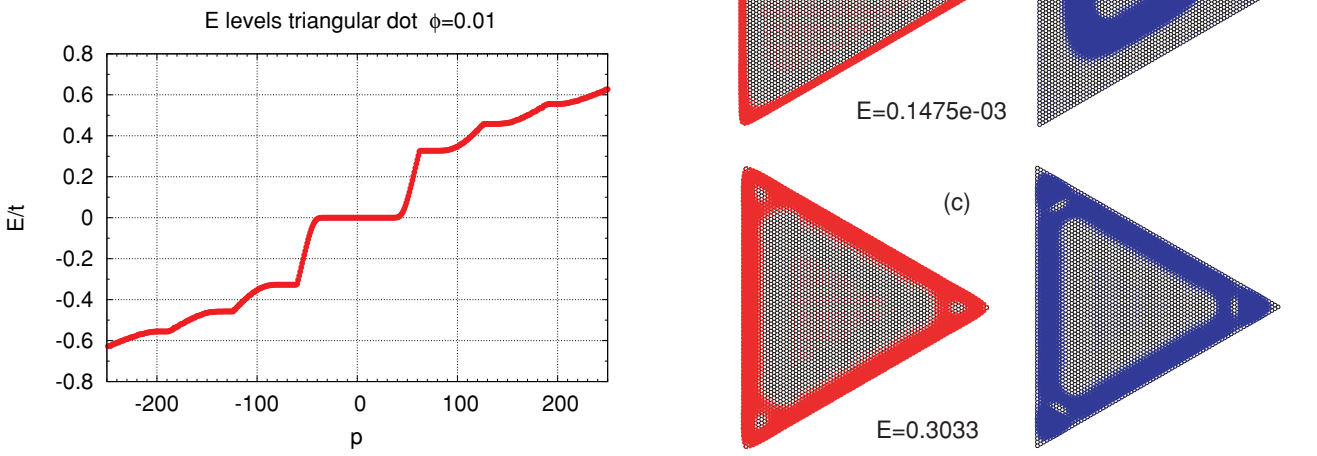

FIG. 5. (Color online) The TB energies at high magnetic field ($\phi = 0.01$) for a triangular flake with zigzag edges comprising $N = 6397$ carbon atoms. The $n = 0$, ±1, ±2, and ±3 Landau levels correspond to the flat segments of the curve. The double-edge states correspond to the rising-in-energy branches between the flat segments. The integer index p counts the TB states (negative p values correspond to negative energies).

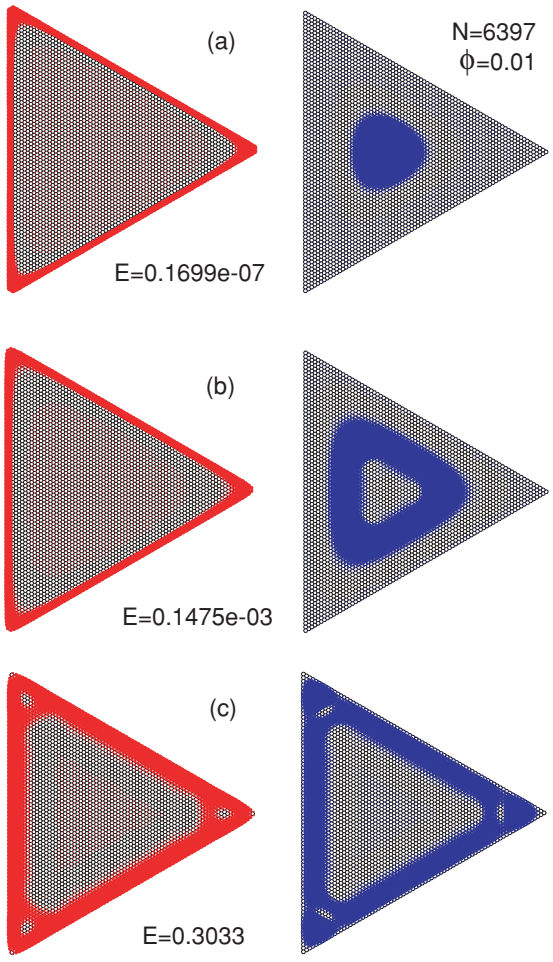

FIG. 6. (Color online) Examples of TB electron densities at high magnetic field ($\phi = 0.01$) for the A (left) and B (right) sublattices associated with: (a) + (b) mixed bulk-edge dispersive states in the $n = 0$ Landau level (whose TB energies reside on the flat step at $E \sim 0$ in Fig. 5). (c) Double-edge states situated on the rising-in-energy branch between the $n = 0$ and $n = 1$ Landau levels. Energies in units of the hopping coupling parameter t.

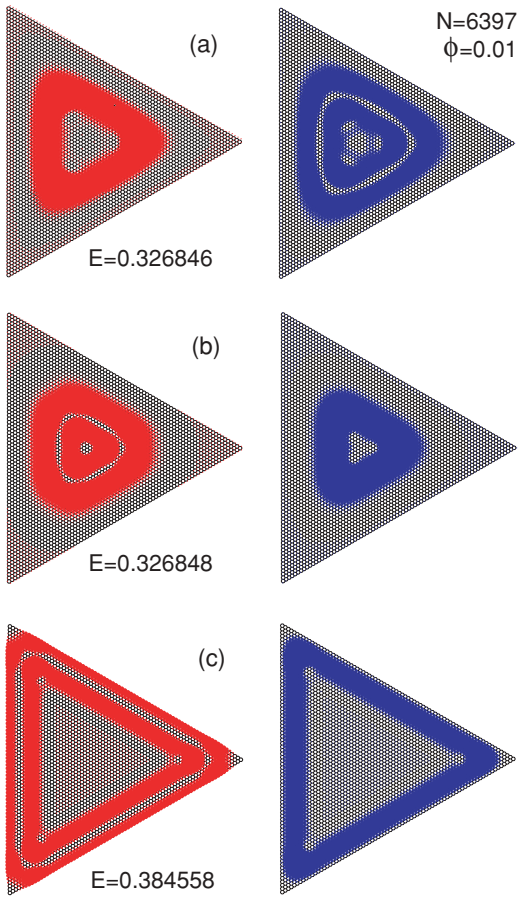

FIG. 7. (Color online) Examples of TB electron densities at high magnetic field ($\phi = 0.01$) for the A (left) and B (right) sublattices associated with: (a) + (b) double-bulk states in the $n = 1$ Landau level. (c) Double-edge states situated on the rising-in-energy branch between the $n = 1$ and $n = 2$ Landau levels. Energies in units of the hopping coupling parameter t.

densities in Figs. 6(a) and 6(b) agrees well with the surface-state Dirac-spinor component in Eq. (11); see also Fig. 4 (bottom frame). Moreover, the profiles of the TB densities for the B sublattices in these figures exhibit the qualitative behavior of a $D_\nu[\sqrt{2}(x - x_c)]$ function with $\nu \gtrsim 0$ described in Sec. II A; see also Fig. 4 (top frame). Note that a lower TB energy [case of Fig. 6(a)] corresponds to a continuous $D_\nu[\sqrt{2}(x - x_c)]$ state with a larger centroid $x_c > 0$, farther away from the physical edge. For states with higher TB energies, lying on the rising-in-energy branch, the B-sublattice component moves toward the physical edge and transforms into an edge state, as illustrated by the double-edge TB state in Fig. 6(c) (with energy $E/t = 0.3033$).

In Figs. 7(a) and 7(b), we portray TB densities for two states associated with the second Landau level (with index $n = 1$ at an energy $E/t \approx 0.326\,85$). Figure 7(a) corresponds to a Dirac spinor in the K valley having an A component consisting of a $D_0(\xi)$ state (no nodes inside the graphene flake) and a B component consisting of a $D_1(\xi)$ state (a single node inside the graphene flake). Figure 7(b) portrays a similar TB state in the K' valley, since the A and B sublattices correspond to the continuous functions $D_1(\xi)$ and $D_0(\xi)$, respectively, which is the opposite from the K-valley case in Fig. 7(a); see Sec. II A 2. Figure 7(c) portrays a double-edge state with energy $E/t = 0.384\,558$ (lying in Fig. 5 on the rising-in-energy branch between the $n = 1$ and $n = 2$ Landau levels). It is apparent that this double-edge TB state is associated with the K' valley and has been evolved out of the double-bulk state in Fig. 7(b); note the preservation of the single node (no node) topology in the A-sublattice (B-sublattice) electron-density component.

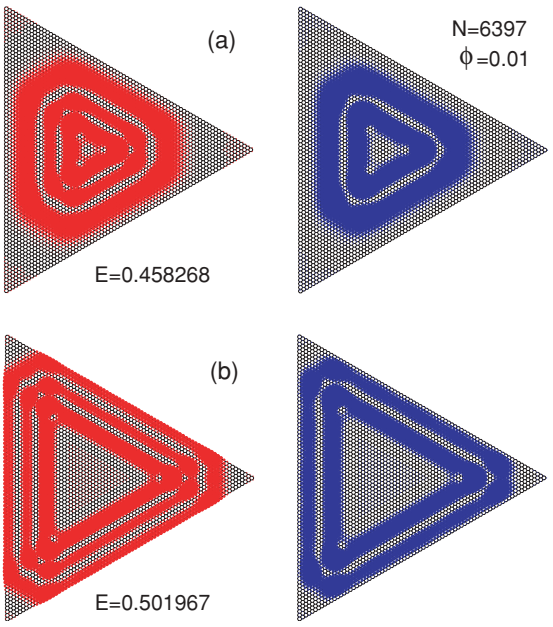

FIG. 8. (Color online) Examples of TB electron densities at high magnetic field ($\phi = 0.01$) for the A (left) and B (right) sublattices of a triangular flake with $N = 6397$ carbon atoms and zigzag edges. (a) Double-bulk states in the $n = 2$ Landau level. (b) Double-edge states situated on the rising-in-energy branch between the $n = 2$ and $n = 3$ Landau levels. Energies in units of the hopping coupling parameter t.

In Fig. 8(a), we portray TB densities for a double-bulk state associated with the third Landau level (with index $n = 2$ at an energy $E/t \approx 0.458\,268$; see Fig. 5). The TB densities in Fig. 8(a) correspond to a continuous Dirac spinor in the K' valley having an A component consisting of a $D_2(\xi)$ state (two nodes inside the graphene flake) and a B component consisting of a $D_1(\xi)$ state (a single node inside the graphene flake); see Sec. II A 2 and Fig. 2 [but with B replaced by A′ and A replaced by B′ (online: blue ↔ red)]. Figure 8(b) portrays a double-edge state with energy $E/t = 0.501\,967$ (lying in Fig. 5 on the rising-in-energy branch between the $n = 2$ and $n = 3$ Landau levels). It is apparent that this double-edge TB state is associated also with the K' valley and has been evolved out of the double-bulk state in Fig. 8(a); note the preservation of the two-node (single-node) topology in the A-sublattice (B-sublattice) electron-density component. Note the similarities with the double-edge continuous Dirac spinor within the physical semi-infinite graphene plane portrayed in Fig. 3.

B. Hexagonal graphene flakes

In Sec. III A, we studied the nature of the TB states in the case of a trigonal flake with zigzag edge terminations.

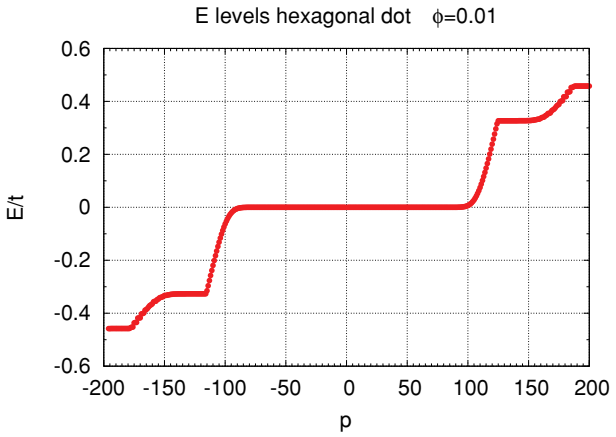

FIG. 9. (Color online) The TB energies at high magnetic field ($\phi = 0.01$) for an hexagonal graphene flake with zigzag edges comprising $N = 6144$ carbon atoms. The $n = 0, \pm 1$, and ± 2 Landau levels correspond to the flat segments of the curve. The double-edge states correspond to the rising-in-energy branches between the flat segments. The integer index p counts the TB states (negative p values correspond to negative energies).

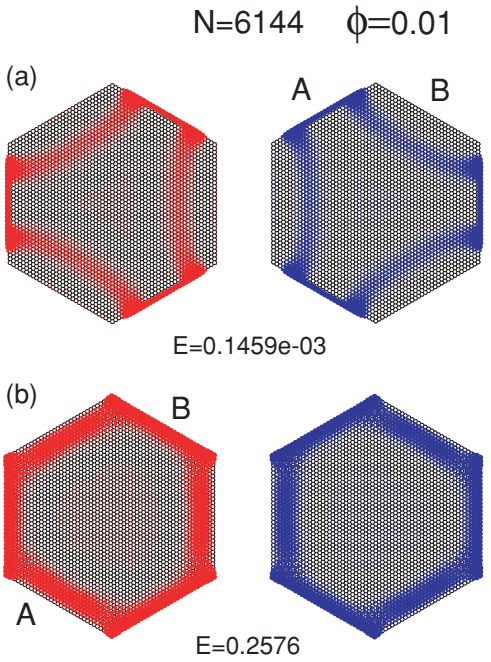

FIG. 10. (Color online) Examples of TB electron densities at high magnetic field ($\phi = 0.01$) for the A (left) and B (right) sublattices of an hexagonal flake with $N = 6144$ carbon atoms and zigzag edges. (a) A mixed bulk-edge state in the $n = 0$ Landau level. (b) A double-edge state with energy situated on the rising-in-energy branch between the $n = 0$ and $n = 1$ Landau levels. The labels A and B indicate the (alternating) sublattice-type edge termination along the sides forming the physical boundary of the hexagon. Energies in units of the hopping coupling parameter t.

A characteristic property of triangular flakes is that the same sublattice participates in the edge terminations of two adjacent polygonal sides (forming an angle of 60°). In this section, we study hexagonal graphene flakes[23] with zigzag edge terminations, which is a more complicated case. This is due to the fact that the sublattices A and B alternate in providing the edge termination of adjacent polygonal sides (having an angle of 120°).

In Fig. 9, we display the TB energies for an hexagonal flake with $\phi = 0.01$ (corresponding to a high magnetic field where Landau levels have been formed). As was the case with the trigonal TB energies in Fig. 5, the TB-energy curve in Fig. 9 exhibits also a well defined trend, i.e., several almost-flat horizontal segments which are connected via fast-varying (rising-in-energy) branches. The flat segments correspond to the Landau levels with energies $E \propto \mathrm{sign}(n)\sqrt{|n|}$, $n = 0, \pm 1, \pm 2, \ldots$.

Furthermore, as was also the case with the trigonal flakes, a close inspection of the properties and behavior of the states associated with the TB energies in the $n = 0$ level in Fig. 9 reveals that this level contains two different bands: (i) a nondispersive one with energies close to the available machine precision ($E/t \sim 10^{-14}$) [that correspond to the $\varepsilon = 0$ solutions of the continuous model; see Sec. II A] and (ii) a quasidegenerate dispersive band with energies that are still very small (starting at $E/t \sim 10^{-6}$) but increase gradually and then merge with the rising energy branch; this band corresponds [see the transcendental Eq. (9)] to the $\varepsilon \gtrsim 0$ solutions of the continuous model in the flat region of the lowest curve (i.e., in the LLL) in Fig. 1(a). Here, we study these dispersive states in the LLL that are formed due to the presence of the magnetic field.

In Fig. 10, we display the TB electron densities (specifically the square root of the densities[36]) for states associated with the LLL in the case of an hexagonal graphene flake under the same magnetic field $\phi = 0.01$. The electron densities of the A (left, online red) and B (right, online blue) sublattices are plotted separately. Figure 10(a) corresponds to a TB state with energy ($E/t = 0.1459 \times 10^{-3}$) that lies well inside the flat segment of the LLL ($n = 0$) energy curve in Fig. 9. This state is of a mixed bulk-edge character, exhibiting, however, a more complex profile compared to the corresponding mixed bulk-edge states for the trigonal flake in Figs. 6(a) and 6(b). This is due to the alternation of the A and B sublattices along the polygonal sides forming the edge of the hexagonal flake. In particular, focusing on a side with a B-sublattice termination (e.g., the one at the upper-right corner), one sees that the A-sublattice density (left, online red) exhibits an edge-state behavior, while the B-sublattice density (right, online blue) exhibits a bulk-state profile. Focusing on a side with an A-sublattice termination (e.g., the one at the lower-left corner), one sees the opposite, i.e., the A-sublattice density (left, online red) exhibits a bulk-state behavior, while the B-sublattice density (right, online blue) exhibits an edge-state profile. In the continuous relativistic Dirac-Weyl model (Sec. II A), the former case is associated with spinor components in the K valley (permitting the vanishing of χ_B on the edge; see Sec. II A 1), while the latter is associated with spinor components in the K' valley (permitting the vanishing of χ'_A on the edge; see Sec. II A 2).

Figure 10(b) displays the TB densities for states with a higher TB energy, $E/t = 0.2576$, lying on the rising-in-energy branch between the $n = 0$ and $n = 1$ Landau levels in Fig. 9.

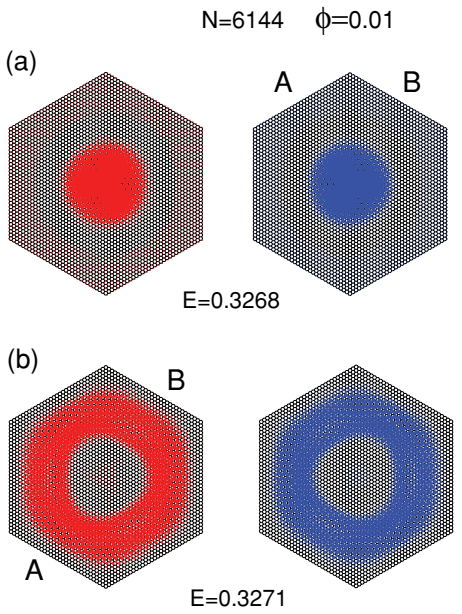

FIG. 11. (Color online) Examples of TB electron densities at high magnetic field ($\phi = 0.01$) for the A (left) and B (right) sublattices of an hexagonal flake with $N = 6144$ carbon atoms and zigzag edges. Both rows [(a) and (b)] portray double-bulk spinors in the $n = 1$ Landau level. The labels A and B indicate the (alternating) sublattice-type edge termination along the sides forming the physical boundary of the hexagon. Energies in units of the hopping coupling parameter t.

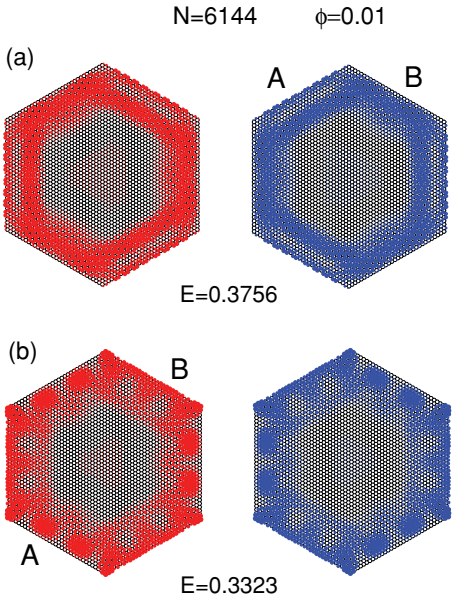

FIG. 12. (Color online) Examples of TB electron densities at high magnetic field ($\phi = 0.01$) for the A (left) and B (right) sublattices of an hexagonal flake with $N = 6144$ carbon atoms and zigzag edges. Both rows [(a) and (b)] portray double-edge spinors with energies in the rising-in-energy branch between the $n = 1$ and $n = 2$ Landau level. The labels A and B indicate the (alternating) sublattice-type edge termination along the sides forming the physical boundary of the hexagon. Energies in units of the hopping coupling parameter t.

This state represents a double-edged one and it can be interpreted as having continuously evolved form the state portrayed in Fig. 10(a), with the bulk components having been pushed against the edges.

Figure 11 portrays TB densities for two double-bulk states associated with the second Landau level of the hexagonal flake (with index $n = 1$ at an energy $E/t \approx 0.3270$; see Fig. 9). The sublattice densities in Fig. 11(a) correspond to a TB state with the lowest energy ($E/t \approx 0.3268$) in this Landau level, and they are concentrated around the center of the flake, far away from the edges. In addition, neither one of them (A-sublattice density or B-sublattice density) exhibits any nodes, which seems paradoxical at a first glance for a state belonging to the first Landau level. The explanation can be found in that the edge of the flake has very little influence in this case, which thus corresponds to a nodeless $l = 0$ Dirac-Weyl state of the $n = 1$ LL in a circular graphene dot with zigzag termination; see Eqs. (A.2) and (A.4) in Ref. 17.

Figure 11(b) portrays TB densities for another double-bulk state with energy $E/t = 0.3271$ belonging to the second ($n = 1$) Landau level of the hexagonal flake; see Fig. 9. The density profiles in Fig. 11(b) exhibit a zero-node and a one-node structure in analogy with the $D_0(\xi)$ and $D_1(\xi)$ functions describing the $n = 1$ Landau level in the continuous Dirac-Weyl model (see Sec. II A). However, in contrast to the single-edge semiinfinite graphene plane in Sec. II A, in Fig. 11(b) the zero-node/one-node topology is present in both sublattices (in both the left and right panels) due to the alternation of the edge termination along the hexagon's sides between the A and B sublattices.

Figure 12 portrays TB densities for two double-edge states whose energies lie on the rising-in-energy branch between the $n = 1$ and $n = 2$ Landau levels; see Fig. 9. The sublattice densities in Fig. 12(a) correspond to a TB state with energy $E/t = 0.3756$. It is apparent that they can be viewed as having evolved out of the densities in Fig. 11(b), with the centroids of the bulk densities having been pushed against the hexagonal edges. Remarkably, at the same time, the zero-node/one-node alternating nodal topology is preserved in the double-edge state in Fig. 12(a) in complete analogy with the double-bulk state in Fig. 11(b).

The sublattice densities in Fig. 12(b) correspond to a TB state with energy $E/t = 0.3323$; they also represent a double-edge state like the one in Fig. 12(a). However, a new characteristic [compared to the double-edge state in Fig. 12(a)] is the appearance of an additional nodal pattern resulting from wave-function quantization along (and parallel to) the hexagon's sides. This additional pattern is superimposed on the perpendicular-to-the-edge zero-node/one-node pattern (the latter being present already in the continuous Dirac-Weyl model of a semiinfinite graphene plane studied in Sec. II A). We note that such combined parallel-to and perpendicular-to-the-edge nodal patterns (not shown) have been found by us also in several instances of TB states in the case of a trigonal graphene flake in Sec. III A.

C. Square graphene flakes

In this section, we study the more complicated case of a square graphene flake which necessarily has mixed

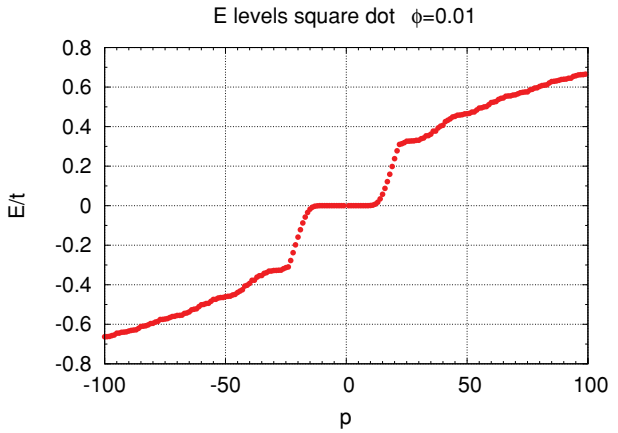

FIG. 13. (Color online) The TB energies at high magnetic field ($\phi = 0.01$) for a square graphene flake with both zigzag and armchair edges comprising $N = 2074$ carbon atoms. The lowest ($n = 0$) Landau level corresponds to the flat segment of the curve at $E \approx 0$. The integer index p counts the TB states (negative p values correspond to negative energies).

armchair and zigzag edge terminations (each type of termination developing on opposite sides of the square). In Fig. 13, we display the TB energies for such a square flake with $\phi = 0.01$ as in the previous studied cases of trigonal (Sec. III A) and hexagonal flakes (Sec. III B). Compared to the energy curves in the previous cases [trigonal (see Fig. 5) and hexagonal (see Fig. 9)], the TB energies in Fig. 13 exhibit higher Landau levels (horizontal segments in Fig. 13) with $n \geqslant 1$ that are not as well formed; this may be due to the smaller number of carbon atoms in the square flake ($N = 2074$). The LLL ($n = 0$) level, however, is well formed, and this is sufficient for our purposes here, namely to investigate whether the mixed LLL bulk-edge states maintain in the presence of edge segments with armchair termination.

Indeed, the TB sublattice densities for the LLL state (with energy $E/t = 0.2769 \times 10^{-2}$) portrayed in Fig. 14 show that the mixed LLL bulk-edge behavior maintains also in the case of a square flake. Naturally, due to the coupling between the K and K' valleys induced by the presence of the armchair terminations, each sublattice [A (online red) and B (online blue)] exhibits now both edge and bulk density contributions, which, however, correspond to different valleys as explicitly marked in Fig. 14.

Mixed bulk-edge states of a square graphene flake in a perpendicular magnetic field were also reported in a recent study.[26] In this study the appearance of such mixed states with significant weight at the zigzag edges were attributed to the coupling between the K and K' valleys due to the armchair edges (see in particular Sec. IV in Ref. 26). This interpretation differs from the conclusion presented in our article where the occurrence of mixed bulk-edge LLL states is shown to originate solely from the zigzag edge termination.

IV. SUMMARY AND DISCUSSION

The properties of single-electron states in graphene flakes with zigzag edge termination under high magnetic fields

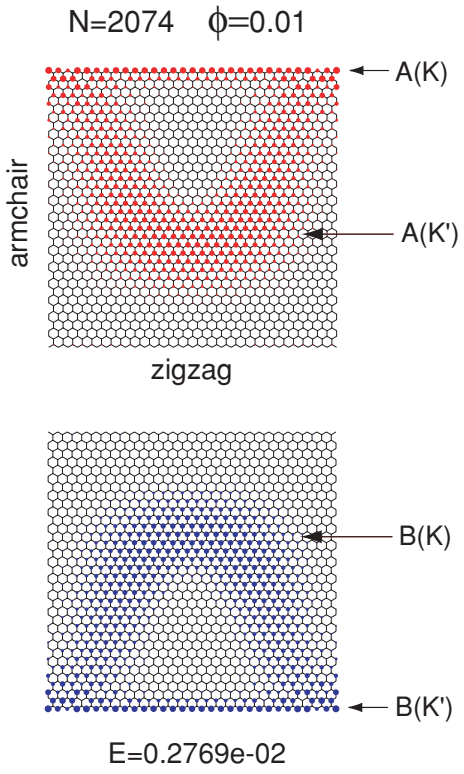

FIG. 14. (Color online) Example of TB electron densities at high magnetic field ($\phi = 0.01$) for the A (online red; top frame) and B (online blue; bottom frame) sublattices of a square flake with $N = 2074$ carbon atoms and both zigzag and armchair edges. A state representing a mixed bulk-edge state in the LLL is displayed. The density contributions on each sublattice associated with a given valley are also marked. Energies in units of the hopping coupling parameter t.

(in the regime of Landau-level formation) were investigated using tight-binding calculations. A systematic interpretation of their character (bulklike versus edgelike) was achieved via a comparison of the tight-binding electron densities with analytic expressions (based on parabolic cylinder functions) for the relativistic Dirac-Weyl spinors in the case of a semi-infinite graphene plane. A variery of graphene flakes was considered, namely trigonal, hexagonal, and square ones.

The higher Landau levels were found to comprise exclusively electrons of bulk-type character (for both sublattices). Furthermore, electrons with energies on the rising-in-energy branches (connecting the Landau levels) are described by edge-type states reminiscent of those familiar from the theory of the integer quantum Hall effect for nonrelativistic electrons. In contrast, in all cases studied, the lowest ($n = 0$) Landau level contained relativistic Dirac electrons of a mixed bulk-edge character without an analog in the nonrelativistic case. Most importantly, it was shown that such mixed bulk-edge states maintain also in the case of a square flake with combined zigzag and armchair edge terminations.

The presence of mixed bulk-edge LLL states in graphene samples with realistic shapes points at significant implications concerning the many-body correlated FQHE excitations. We recall that Ref. 17 studied the many-body correlated FQHE excitations in the LLL in the simplified case of a circular

graphene flake with zigzag edge termination, and it found that the two-body Coulomb-interaction matrix elements are given as a sum of four terms

$$\tfrac{1}{4}(\langle\tilde{b}_1\tilde{b}_2|\tilde{b}_3\tilde{b}_4\rangle + \langle\tilde{e}_1\tilde{e}_2|\tilde{e}_3\tilde{e}_4\rangle + \langle\tilde{b}_1\tilde{e}_2|\tilde{b}_3\tilde{e}_4\rangle + \langle\tilde{e}_1\tilde{b}_2|\tilde{e}_3\tilde{b}_4\rangle), \tag{21}$$

where $|\tilde{b}\rangle$ and $|\tilde{e}\rangle$ denote the bulk and edge components of the mixed LLL state; note that, due to the equal weights (50–50%) of the bulklike and edgelike components, a prefactor of $1/4$ appears in front of each term in Eq. (21). As a consequence of Eq. (21) and of the $1/4$ prefactor, a sizable attenuation of the many-body correlated FQHE excitations in the LLL (associated with the $\langle\tilde{b}_1\tilde{b}_2|\tilde{b}_3\tilde{b}_4\rangle/4$ term reflecting the depletion of the bulk component) was found in the simplified case of a circular graphene flake. Furthermore, it was shown[17] that the insulating behavior at the Dirac neutrality point under high B (experimentally observed[18,19] in graphene samples along with the $1/3$ FQHE) is associated with the Coulombic repulsion due to the accumulation of charge at the edges [related to the $\langle\tilde{e}_1\tilde{e}_2|\tilde{e}_3\tilde{e}_4\rangle/4$ and the remaining two cross terms in the Coulomb-interaction matrix elements given in Eq. (21)].

The current study shows that the appearance of mixed bulk-edge LLL states is a property of the presence of segments in the graphene-sample boundary having a zigzag edge termination, independent of the precise shape of the graphene sample. This finding suggests that the results of Ref. 17 concerning the many-body correlated FQHE excitations in the LLL can be generalized to graphene samples with more realistic shapes.

ACKNOWLEDGMENTS

This work was supported by the Office of Basic Energy Sciences of the U.S. D.O.E. under contract FG05-86ER45234.

*Igor.Romanovsky@gatech.edu
†Constantine.Yannouleas@physics.gatech.edu
‡Uzi.Landman@physics.gatech.edu

[1] K. S. Novoselov, A. K. Geim, S. V. Morozov, D. Jiang, Y. Zhang, S. V. Dubonos, I. V. Grigorieva, and A. A. Firsov, Science **306**, 666 (2004).
[2] C. Berger, Z. M. Song, T. B. Li, X. B. Li, A. Y. Ogbazghi, R. Feng, Z. T. Dai, A. N. Marchenkov, E. H. Conrad, P. N. First, and W. A. de Heer, J. Phys. Chem. B **108**, 19912 (2004).
[3] M. Fujita, K. Wakabayashi, K. Nakada, and K. Kusakabe, J. Phys. Soc. Jpn. **65**, 1920 (1996).
[4] K. Nakada, M. Fujita, G. Dresselhaus, and M. S. Dresselhaus, Phys. Rev. B **54**, 17954 (1996).
[5] K. Wakabayashi, M. Fujita, H. Ajiki, and M. Sigrist, Phys. Rev. B **59**, 8271 (1999).
[6] Y. W. Son, M. L. Cohen, and S. G. Louie, Phys. Rev. Lett. **97**, 216803 (2006).
[7] L. Brey and H. A. Fertig, Phys. Rev. B **73**, 235411 (2006).
[8] D. A. Abanin, P. A. Lee, and L. S. Levitov, Phys. Rev. Lett. **96**, 176803 (2006).
[9] A. H. Castro Neto, F. Guinea, N. M. R. Peres, K. S. Novoselov, and A. K. Geim, Rev. Mod. Phys. **81**, 109 (2009).
[10] L. C. Campos, V. R. Manfrinato, J. D. Sanchez-Yamagishi, J. Kong, and P. Jarillo-Herrero, Nano Lett. **9**, 2600 (2009).
[11] X. Jia, M. Hofmann, V. Meunier, B. G. Sumpter, J. Campos-Delgado, J. M. Romo-Herrera, H. Son, Y.-P. Hsieh, A. Reina, J. Kong, M. Terrones, and M. S. Dresselhaus, Science **323**, 1701 (2009).
[12] S. Neubeck, Y. M. You, Z. H. Ni, P. Blake, Z. X. Shen, A. K. Geim, and K. S. Novoselov, Appl. Phys. Lett. **97**, 053110 (2010).
[13] L. P. Biró and Ph. Lambin, Carbon **48**, 2677 (2010).
[14] E. Cruz-Silva, A. R. Botello-Mendez, Z. M. Barnett, X. Jia, M. S. Dresselhaus, H. Terrones, M. Terrones, B. G. Sumpter, and V. Meunier, Phys. Rev. Lett. **105**, 045501 (2010).
[15] R. Yang, L. Zhang, Y. Wang, Z. Shi, D. Shi, H. Gao, E. Wang, and G. Zhang, Adv. Mater. **22**, 4014 (2010).
[16] B. Krauss, P. Nemes-Incze, V. Skakalova, L. P. Biró, K. von Klitzing, and J. H. Smet, Nano Lett. **10**, 4544 (2010).
[17] C. Yannouleas, I. Romanovsky, and U. Landman, Phys. Rev. B **82**, 125419 (2010).
[18] X. Du, I. Skachko, F. Duerr, A. Luican, and E. Y. Andrei, Nature (London) **462**, 192 (2009).
[19] K. I. Bolotin, F. Ghahari, M. D. Shulman, H. L. Stormer, and Ph. Kim, Nature (London) **462**, 196 (2009).
[20] W. Bao, Z. Zhao, H. Zhang, G. Liu, Ph. Kratz, L. Jing, J. Velasco, Jr., D. Smirnov, and C. N. Lau, e-print arXiv:1005.0033v1.
[21] J. G. Checkelsky, L. Li, and N. P. Ong, Phys. Rev. Lett. **100**, 206801 (2008).
[22] For earlier works concerning in particular the properties of the energy spectrum at $B = 0$ of graphene flakes with triangular, hexagonal, or rectangular shapes, see, e.g., J. Fernandez-Rossier and J. J. Palacios, Phys. Rev. Lett. **99**, 177204 (2007); M. Ezawa, Phys. Rev. B **76**, 245415 (2007); O. Hod, V. Barone, and G. E. Scuseria, *ibid.* **77**, 035411 (2008); C. Tang, W. Yan, Y. Zheng, G. Li, and L. Li, Nanotechnology **19**, 435401 (2008); H. P. Heiskanen, M. Manninen, and J. Akola, New J. Phys. **10**, 103015 (2008); A. V. Rozhkov and F. Nori, Phys. Rev. B **81**, 155401 (2010); D. P. Kosimov, A. A. Dzhurakhalov, and F. M. Peeters, *ibid.* **81**, 195414 (2010). For studies at finite B, see also Refs. 23–27.
[23] Z. Z. Zhang, K. Chang, and F. M. Peeters, Phys. Rev. B **77**, 235411 (2008).
[24] D. A. Bahamon, A. L. C. Pereira, and P. A. Schulz, Phys. Rev. B **79**, 125414 (2009).
[25] M. Wimmer, A. R. Akhmerov, and F. Guinea, Phys. Rev. B **82**, 045409 (2010).
[26] S. C. Kim, P. S. Park, and S.-R. Eric Yang, Phys. Rev. B **81**, 085432 (2010).
[27] F. Libisch, S. Rotter, J. Güttinger, C. Stampfer, and J. Burgdörfer, Phys. Rev. B **81**, 245411 (2010).
[28] E. W. Weisstein, *Parabolic Cylinder Function*, from MathWorld [http://mathworld.wolfram.com/ParabolicCylinderFunction.html].
[29] M. Abramowitz and I. A. Stegun, eds., *Handbook of Mathematical Functions* (National Bureau of Standards, Washington, DC, 1972).
[30] B. I. Halperin, Phys. Rev. B **25**, 2185 (1982).
[31] The parabolic cylinder functions were also used to determine the energy spectrum of the semi-infinite graphene half-plane under a

perpendicular magnetic field in V. P. Gusynin, V. A. Miransky, S. G. Sharapov, and I. A. Shovkovy, Phys. Rev. B **77**, 205409 (2008).

[32]The ceiling function is defined as $\lceil \nu \rceil = n + 1$, if $n < \nu \leqslant n + 1$ with n being an integer.

[33]In the current article, we consider the TB Hamiltonian for finite graphene flakes with nearest-neighbor hopping. Perturbing effects from more distant neighbors, i.e., second[9,25] and third (see S. Reich, J. Maultzsch, C. Thomsen, and P. Ordejón, Phys. Rev. B **66**, 035412 (2002) and Ref. 27) have also been discussed. The second nearest-neighbor hopping term in the TB Hamiltonian introduces a perturbation that breaks the electron-hole symmetry. Consequently, inclusion of this term may change the bulk-to-edge ratio in the LLL mixed states. Recall that for a Hamiltonian that preserves the electron-hole symmetry the bulk and edge components in the LLL mixed state have equal weights.[17] Furthermore the third nearest-neighbor hopping term preserves the electron-hole symmetry. From the above we conclude that to assess the precise extent of the effect of higher-order neighbors on the mixed bulk-edge states deserves a future study. Note that while the second-nearest-neighbor hopping term is (at least) an order of magnitude smaller than the nearest-neighbor one, it is of the same order of magnitude (or smaller) as the third-nearest-neighbor term (see S. Reich *et al.* above and C. Bena and L. Simon, e-print arXiv:1007.3907).

[34]R. B. Lehoucq, D. C. Sorensen, and C. Yang, *ARPACK Users' Guide: Solution of Large-Scale Eigenvalue Problems with Implicitly Restarted Arnoldi Methods* (SIAM, Philadelphia, 1998).

[35]D. R. Hofstadter, Phys. Rev. B **14**, 2239 (1976).

[36]A scaling factor is used in order to achieve the best legibility of the figures.